The Astrophysical Journal, 962:185 (10pp), 2024 February 20 https://doi.org/10.3847/1538-4357/ad1dd6

Ultra–short-period WD Binaries Are Not Undergoing Strong Tidal Heating

Peter Scherbak[1] and Jim Fuller[2]
[1] California Institute of Technology, Astronomy Department, Pasadena, CA 91125, USA
[2] TAPIR, California Institute of Technology, Pasadena, CA 91125, USA
Received 2023 November 6; revised 2024 January 2; accepted 2024 January 10; published 2024 February 20

Abstract

Double white dwarf (WD) binaries are increasingly being discovered at short orbital periods where strong tidal effects and significant tidal heating signatures may occur. We assume that the tidal potential of the companion excites outgoing gravity waves within the WD primary, the dissipation of which leads to an increase in the WD's surface temperature. We compute the excitation and dissipation of the waves in cooling WD models in evolving MESA binary simulations. Tidal heating is self-consistently computed and added to the models at every time step. As a binary inspirals to orbital periods less than ∼20 minutes, the WD's behavior changes from cooling to heating, with temperature enhancements that can exceed 10,000 K compared with nontidally heated models. We compare a grid of tidally heated WD models to observed short-period systems with hot WD primaries. While tidal heating affects their $T_{\rm eff}$, it is likely not the dominant luminosity. Instead, these WDs are probably intrinsically young and hot, implying that the binaries formed at short orbital periods. The binaries are consistent with undergoing common envelope evolution with a somewhat low efficiency $\alpha_{\rm CE}$. We delineate the parameter space where the traveling wave assumption is most valid, noting that it breaks down for WDs that cool sufficiently, where standing waves may instead be formed.

Unified Astronomy Thesaurus concepts: White dwarf stars (1799); Tidal interaction (1699); Close binary stars (254); Stellar evolutionary models (2046); Common envelope evolution (2154)

1. Introduction

Double white dwarf (DWD) binaries have increasingly been found at short orbital periods (e.g., Brown et al. 2011; Burdge et al. 2020b), with the tightest detached system at an orbital period of only 6.9 minutes (Burdge et al. 2019). For these compact systems, tides are expected to be very strong (e.g., Iben et al. 1998), but the effects of tides on the WDs and the resulting observable predictions have remained uncertain.

As DWD binaries inspiral to shorter orbital separations owing to the emission of gravitational waves (GWs), tidal effects will become stronger, and tidal heating could become the dominant source of luminosity (Iben et al. 1998; Burdge et al. 2020a). Measuring tidal heating is one of the principle ways to constrain tidal physics (Piro 2019). At very short periods, tides may affect the premerger conditions of DWD binaries, such as the synchronization of WD rotation with the binary orbit. The degree of synchronization premerger is unclear, with some simulations assuming that the WDs are tidally locked (e.g., Raskin et al. 2012; Dan et al. 2014), whereas others have assumed that the WDs are initially nonrotating (e.g., Yoon et al. 2007; Lorén-Aguilar et al. 2009). When comparing WD merger simulations with these two different initial conditions, Dan et al. (2014) found that the merger timescale and the location of helium detonation were significantly altered. Therefore, the degree of synchronization seems to affect the merger product of two WDs, which is a pathway to Type Ia supernovae (e.g., Shen 2015) and other exotic phenomena.

While tides are expected to contribute to heating of both WDs, quantitative predictions of the heating, as well as its dependence on WD mass and system orbital period, have not been rigorously performed. Instead, the magnitude of the tidal heating has only been estimated for a few different WD masses and orbital periods (Fuller & Lai 2013; Yu et al. 2021), and the changing WD structure, heating rate, and location of heat deposition have not been self-consistently modeled. Many recently discovered short-period DWD binaries have measured masses and surface temperatures, meaning that precise predictions of tidal heating can now be directly compared to observations.

In a compact binary, each component feels a tidal force due to its companion's gravitational potential. The equilibrium tidal response, referring to a body's overall deformation in quasi-static equilibrium, is unlikely to be important except when the binary is close to mass-transferring (Fuller & Lai 2011). Rather, the wavelike or oscillatory tidal response, known as the dynamical tide (Zahn 1975, 1977), is likely dominant. The dynamical tide often involves the excitation of standing-wave gravity modes (Zahn 2008), or, if there is sufficient dissipation, a train of traveling gravity waves (Goldreich & Nicholson 1989). In stars on the main sequence, waves are excited at the convective–radiative boundary, and their dissipation can drive circularization and synchronization of the binary. Gravity modes are also found in WDs, as demonstrated observationally by pulsating ZZ Ceti stars (Brickhill 1983). The nature of the tidal excitation and whether it is in the standing-wave or traveling-wave regime will help determine the impact of tides on a WD's observed properties. Previous works that have focused on standing waves in WDs include Burkart et al. (2013) and Yu et al. (2020).

In a series of papers, Fuller & Lai (2011, 2012, 2013) applied the theory of dynamical tides to a DWD binary. In particular, Fuller & Lai (2012) and Fuller & Lai (2013) found that, for both CO- and He-core WDs, excited gravity modes are likely to damp in the outer envelope and prevent the formation

of standing waves. Fuller & Lai (2013) modeled tidal heating in a WD model, but this analysis was limited to a WD model of fixed mass initialized at fixed temperatures.

In this paper, we investigate tidal effects for WDs of various masses that undergo evolution in a binary and are allowed to realistically cool (if tidal heating is unimportant) or be heated by tides. Only with a grid of models can simulations be compared to known systems to better interpret observations. In addition, Fuller & Lai (2013) assumed that the tidal response is in the strongly dissipated traveling-wave regime, and they focused on nonlinear wave breaking as the most important dissipative mechanism. Here we model the contributions of both nonlinear wave breaking and radiative damping as dissipative mechanisms, and we estimate where the overall traveling-wave assumption breaks down.

In this work, we self-consistently implement tidal effects into cooling He-core WD models simulated in the MESA stellar evolutionary code (Paxton et al. 2011, 2013, 2015, 2018, 2019). Section 2 reviews the physics of the excitation of gravity modes/gravity waves in a DWD binary. Section 3 describes the implementation of dynamical tides in a DWD binary MESA simulation, where the WDs undergo spin-up and heating due to the dissipation of excited gravity waves. Section 3.2 presents the models where the traveling-wave response works best and where it breaks down. Section 4 presents tidal heating predictions for simulations of differing WD masses and initial orbital periods and compares these predictions to observed ultra–short-period DWD binaries. We discuss our results in Section 5 and conclude in Section 6.

2. Basic Tidal Physics

More detailed analysis of tidally excited oscillations in WDs is found in Fuller & Lai (2012). Here we review the basic quantities needed for our analysis.

Consider a DWD binary with primary mass M_1 and secondary mass M_2 in a circular orbit of separation a and orbital frequency Ω. The following analysis treats the secondary as a point mass and only models tidal effects in the primary M_1, which has a radius R. The presence of M_2 creates a tidal potential that acts as a forcing term in the fluid equations describing the primary's interior. The tidal potential is predominantly quadrupolar with degree $l = m = 2$. It varies sinusoidally in time with tidal frequency

$$\omega = 2(\Omega - \Omega_s), \tag{1}$$

where Ω_s is the spin frequency of the WD.

In the outer region of the WD, the tidal potential can excite either standing g-modes (with a reflective outer boundary condition) or gravity waves (with an outgoing boundary condition). In either case, the restoring force for these oscillations is buoyancy. The Brunt–Väisälä frequency N, or buoyancy frequency, is therefore very important in determining where these modes/waves are excited and where they can propagate.

Because of strong dissipative effects, the wave energy may be depleted before the wave is reflected. Therefore, in this work we assume that the response is in the outgoing wave regime (but see Section 3.2 and figures therein for when this assumption breaks down). For a He-core WD, the outgoing wave is excited near the composition gradient at the transition between the WD's He core and H envelope (Fuller & Lai 2013), where there is a spike in N^2.

In the Wentzel–Kramers–Brillouin (WKB) limit, gravity waves satisfy the dispersion relation

$$k_{r,\mathrm{WKB}}^2 = \frac{(L_l^2 - \omega^2)(N^2 - \omega^2)}{a_s^2 \omega^2} \tag{2}$$

with the Lamb frequency

$$L_l^2 = \frac{l(l+1)a_s^2}{r^2}, \tag{3}$$

where k_r is the radial wavenumber, a_s is the adiabatic sound speed, and r is the internal radius of the WD. We leave l general in our equations, although $l = 2$ is always assumed in this paper.

In most of the WD's interior, the gravity waves satisfy $\omega^2 \ll L_l^2$ and $\omega^2 \ll N^2$. However, there are regions near the surfaces of our WD models where ω^2 becomes comparable to L_l^2 (see also Section 3.2.1 for how the traveling-wave approximation can break down in these cases). If applied to Equation (2), k_r^2 would become very small. We therefore assume a lower limit of k_r^2 as $1/(4H^2)$, where H is the pressure scale height. Therefore, our full expression for the radial wavenumber is

$$k_r^2 = max\left[(L_l^2 - \omega^2)(N^2 - \omega^2)\Big/ a_s^2\omega^2, \frac{1}{4H^2}\right]. \tag{4}$$

The wave carries both an angular momentum (AM) flux and energy flux toward the surface of the WD. AM and energy will therefore be transferred from the binary orbit to the WD, causing the WD to undergo spin-up and heating.

3. Tidal Effects in MESA Simulations

We create He-core WDs in the MESA stellar evolutionary code (Paxton et al. 2011, 2013, 2015, 2018, 2019). The WD models are created by mass stripping of an evolved red giant branch star when its He core reaches masses of 0.25, 0.30, 0.35, 0.40, and 0.45 $M_\odot$, giving five WD masses in our grid. We varied the mass of hydrogen in these WD models from about 10^{-5} to 10^{-3} $M_\odot$, but we found that our tidal spin-up and tidal heating results were ultimately not greatly affected, with parameters like WD mass and age mattering much more (see Appendix C for further discussion). However, if the hydrogen envelope was completely stripped, we would not expect a spike in Brunt–Väisälä frequency where the gravity waves are excited, and our assumptions would greatly break down. Therefore, our results likely only apply to DA WDs with a hydrogen atmosphere.

We simulate tidal interactions with the WD in a binary MESA simulation with a point-mass companion. The WD is initialized at a hot surface temperature after mass stripping, meant to represent a newly formed WD at the top of its cooling track. We therefore model tidal effects in the younger WD, assuming that the companion WD already exists. If tidal heating is not implemented, the WD cools monotonically. The binary system evolves only as a result of the emission of GWs. The tidal back-reaction of tides on the orbit is not implemented because it is subdominant (Fuller & Lai 2012; Burdge et al. 2019). We initialize the binaries at a range of initial orbital periods, which represents the birth period of the DWD binary, i.e., when the younger WD formed. It also corresponds to the post–common envelope (post-CE) period of the binary, as these DWDs likely went through CE evolution (e.g., Nelemans & Tout 2005).

3.1. WD Spin-up

We assume that the WD is rigidly rotating and therefore has a constant Ω_s from surface to core (the validity of this assumption is discussed in Appendix A). Fuller & Lai (2013) find that the tidal torque $\dot{J}_z$ can be written as

$$\dot{J}_z = T_0 F(\omega). \tag{5}$$

Here $T_0 = GM_2^2 R^5/a^6$ and represents how the magnitude of the tidal forcing scales with the binary system parameters. $F(\omega)$ quantifies the strength of the excited wave and is determined by solving for the waveform of tidally excited gravity waves at various frequencies. The numerical solver developed in Fuller & Lai (2013) calculates the waveform by solving the equations of stellar oscillation with a tidal forcing term, assuming an outgoing boundary condition for the wave. For our WD models of varying mass, we calibrated $F(\omega)$ by running the solver on MESA profiles saved at various ages. We found that $F(\omega)$ approximately scales as

$$F(\omega) = \hat{f}\,\hat{\omega}^7, \tag{6}$$

where $\hat{\omega}$ is ω in units of $\sqrt{GM/R^3}$ and $\hat{f}$ is a function of WD mass and age. This power-law scaling is slightly steeper than that found in Fuller & Lai (2013), where $F(\omega) = \hat{f}\,\hat{\omega}^6$. However, the values of $\hat{f}$ are similar and increase as the WD ages. We implement an interpolation of $\hat{f}$ into MESA, interpolating as a function of WD mass and age. As a rough estimate, $\hat{f} \approx \hat{f}_0 t_{\rm age}^{0.4}$, where $t_{\rm age}$ is the age of the WD up to $\approx$1 Gyr and $\hat{f}_0 = 3 \times 10^{-6}$ for a 0.35 $M_\odot$ WD. $\hat{f}_0$ is larger (smaller) by a factor of $\approx$3 for a 0.45 (0.25) $M_\odot$ WD.

Given the tidal torque, the spin-up rate of Ω_s is

$$\dot{\Omega}_s = \frac{\dot{J}_z}{I} = \frac{T_0 \hat{f}\,\hat{\omega}^7}{I}, \tag{7}$$

where I is the moment of inertia of the WD. Equations (1) and (7) are coupled and can be numerically solved for Ω_s and ω during the MESA simulation. We assume that the WD starts with $\Omega_s = 0$ at some orbital frequency Ω and then allow the system to evolve. The WD cools, and the binary inspirals to closer separations/higher orbital frequencies owing to the emission of GWs.

The tidal spin-up is shown in Figure 1 for a WD of 0.35 $M_\odot$ starting at orbital periods of 20, 50, and 90 minutes. The WD's spin becomes synchronized with the orbit at short orbital periods ($\Omega_s/\Omega \to 1$). By the time the binaries are at periods $\lesssim$30 minutes, the binaries starting at 50 and 90 minutes are in the synchronizing regime where $\dot{\Omega}_s \approx \dot{\Omega}$. The WD starting in a binary at 20 minutes spins up very rapidly at first because the tidal torque is strong and it is in the short-period regime where synchronization would be expected. However, the young WD's radius also contracts rapidly, leading temporarily to a decreased torque and a dip in the value of Ω_s/Ω, before continuing to approach synchronization at shorter periods.

We find similar behavior for He-core WDs of masses 0.25–0.45 $M_\odot$, where the spin becomes increasingly synchronized with the orbit at orbital periods $\lesssim$30 minutes.

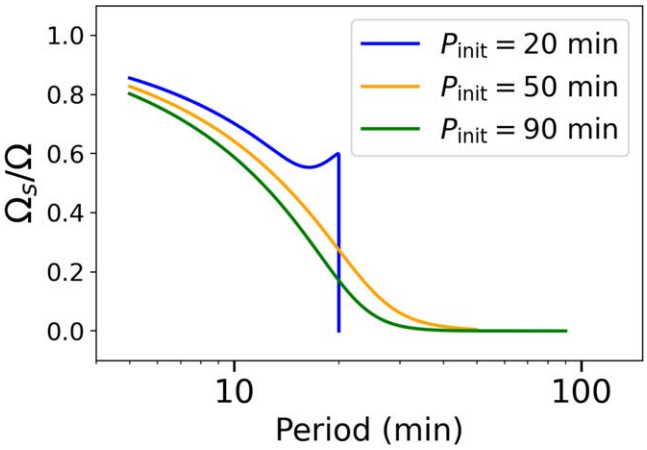

Figure 1. Evolution of the spin frequency Ω_s in units of the orbital frequency Ω as a function of the orbital period, due to tidal synchronization. The WDs start with $\Omega_s = 0$. The WD mass is fixed at 0.35 $M_\odot$, and WD models start evolution at the same temperature, but in a binary with different initial orbital period. The companion mass is fixed at 0.3 $M_\odot$.

3.2. WD Heating

With the evolution of spin frequency Ω_s and tidal frequency ω known, the tidal heating can also be estimated. There are two basic steps to the process: (1) Calculate the magnitude of the power carried by the outgoing gravity wave, $L_{\rm tide}$. (2) Calculate the energy dissipated as heat (therefore lost from the wave) at each mass coordinate m within the WD, between the location of wave excitation and the upper boundary of the wave propagation cavity. The heat is then injected into the WD model via the MESA control `s% extra_heat` (with dimension energy/time/mass). The power $L_{\rm tide}$ carried by the wave in the corotating frame of the WD (for the dominant $m = 2$ component of the tidal response) is

$$L_{\rm tide} = \frac{\omega}{2}\dot{J}_z = \frac{\omega}{2} T_0 F(\omega) \simeq \frac{\omega}{2} T_0 \hat{f}\,\hat{\omega}^7. \tag{8}$$

The next step is to calculate the energy dissipated as heat in each cell of the model as the traveling wave propagates outward. In practice, the gravity wave never reaches the surface of the WD because either its energy is dissipated as heat or the wave reaches the end of its propagation cavity, where either $\omega^2 > L_l^2$ or $\omega^2 > N^2$. Moving outward from the excitation location, energy is removed from the wave via two dissipative mechanisms: nonlinear wave breaking and damping due to radiative diffusion. The decrease in $L_{\rm tide}$ over a cell of mass dm, $dL_{\rm tide}/dm$, is the power per unit mass deposited in a cell, and thus the necessary value for `s% extra_heat`.

If radiative damping alone is included,

$$\frac{dL_{\rm tide}}{dm} = -\frac{L_{\rm tide}}{m_{\rm damp}}, \tag{9}$$

where $m_{\rm damp}$ is the characteristic mass scale for damping. This is related to the wave damping length scale $h_{\rm damp}$ by

$$m_{\rm damp} = 4\pi\rho r^2 h_{\rm damp}, \tag{10}$$

and the length scale for thermal diffusion is

$$h_{\rm damp} = v_g/(k_r^2 K), \tag{11}$$

where $v_g \approx \omega/k_r$ is the group velocity of the wave, ρ is the mass density, and K is the thermal diffusivity (e.g., Fuller 2017). K is

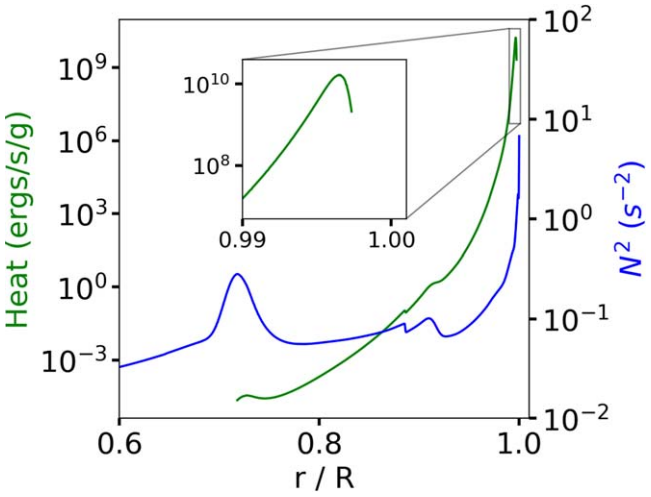

Figure 2. Gravity wave excitation in the outer region of a 0.35 $M_\odot$ WD, plotted vs. the radius r. The outgoing wave is assumed to originate at the bump in the Brunt–Väisälä frequency squared N^2 (blue curve) corresponding to the core-envelope composition gradient. Heating due to wave dissipation (green curve) only takes place at exterior locations to the composition gradient. This snapshot is shown for an orbital period of 14.3 minutes and a companion mass of 0.3 $M_\odot$.

given by

$$K = \frac{16\sigma_{\rm SB}T^3}{3\rho^2\kappa c_p}, \tag{12}$$

where $\sigma_{\rm SB}$ is the Stefan–Boltzmann constant, T is internal temperature, κ is the effective opacity (which includes thermal conduction), and c_p is specific heat at constant pressure.

We assume that radiative damping always operates. In contrast, nonlinear wave breaking is assumed to only occur when the wave reaches a large enough radial displacement ξ_r such that $|\xi_r||k_r| \geqslant 1$. See Appendix B for the calculation of ξ_r. We find that wave breaking only occurs in simulations at orbital periods $\lesssim$15 minutes, with radiative damping providing all the dissipation at longer periods. Similarly, we define $m_{\rm break}$ as the characteristic mass scale for breaking, related to characteristic length scale $h_{\rm break}$ by

$$m_{\rm break} = 4\pi\rho r^2 h_{\rm break}, \tag{13}$$

with $h_{\rm break}$ estimated to be one pressure scale height. Therefore, our full expression for the power deposited per unit mass is

$$\frac{dL_{\rm tide}}{dm} = -\frac{L_{\rm tide}}{m_{\rm damp}} - \frac{L_{\rm tide}}{m_{\rm break}}\Theta(|\xi_r||k_r| - 1), \tag{14}$$

where Θ is simply a Heaviside step function such that wave breaking only contributes when $|\xi_r||k_r| \geqslant 1$.

Figure 2 shows a radial profile for the heat deposited in the outer region of a WD model at a short orbital period. The outgoing wave is assumed to originate at the bump in N^2, so heating only exists exterior to this point. For this snapshot, dissipation is only due to radiative damping. The heating per unit mass reaches a maximum close to the surface of the WD, where N^2 is large and the density is low. This behavior is typical for our simulations.

We remove energy from the wave and deposit it as heat by applying Equation (14) until either $L_{\rm tide}$ is zero from losses or the end of the gravity wave propagation cavity is reached. In the first case, the energy injected into the WD $L_{\rm heat}$ is equal to

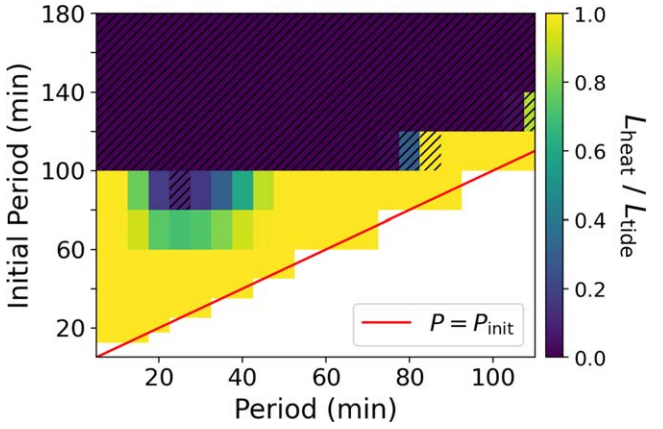

Figure 3. The fraction of the wave energy $L_{\rm tide}$ that is deposited as heat $L_{\rm heat}$ (color shading) within evolving WD models of 0.25 $M_\odot$ (with a 0.3 $M_\odot$ companion). A given simulation starts on the red line and moves from right to left horizontally, toward shorter orbital periods as inspiral occurs. If $L_{\rm heat}/L_{\rm tide}$ is less than unity, the wave is encountering the upper edge of the propagation cavity, where the wave frequency rises above either the Lamb frequency (unhatched region) or the Brunt–Väisälä frequency (hatched region). The traveling-wave approximation is good in the yellow regions of this diagram.

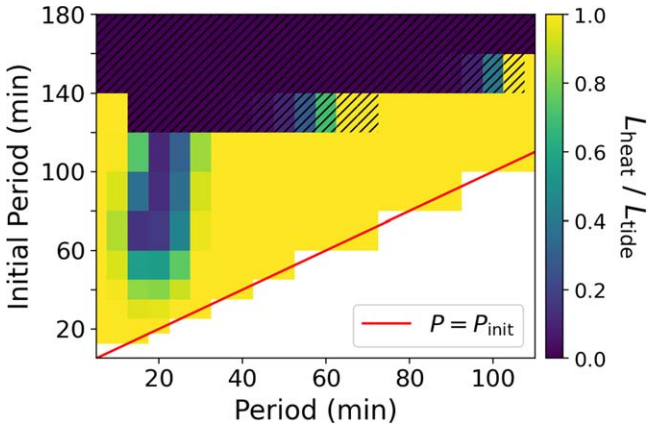

Figure 4. Same as Figure 3, but for a 0.35 $M_\odot$ WD model in a binary.

$L_{\rm tide}$. In the second case, $L_{\rm heat}/L_{\rm tide}$ will be less than unity, meaning that not all the wave's energy is deposited inside our model. If this fraction is significantly less than unity, the wave carries a significant amount of energy when it reaches the edge of the propagation cavity and likely reflects. In this case, the assumption that the tidal response is in the traveling-wave regime breaks down. Instead, standing-wave g-modes of discrete frequencies will likely be excited (Fuller & Lai 2011; Yu et al. 2021).

3.2.1. Traveling-wave Regime: Validity

We do not model the standing-wave regime, but instead estimate for which models our traveling-wave assumption breaks down. For three different WD masses, Figures 3, 4, and 5 show a color map of $L_{\rm heat}/L_{\rm tide}$ versus the parameter space of initial period and orbital period. A given simulation has a fixed initial period but decreases in period, starting on the red line and moving horizontally right to left. A brighter color corresponds to $L_{\rm heat}/L_{\rm tide}$ being closer to unity and the traveling-wave assumption being justified. When $L_{\rm heat}/L_{\rm tide}$ is close to zero, with a darker shading, our model likely breaks down. As a model moves from right to left on the plot, the

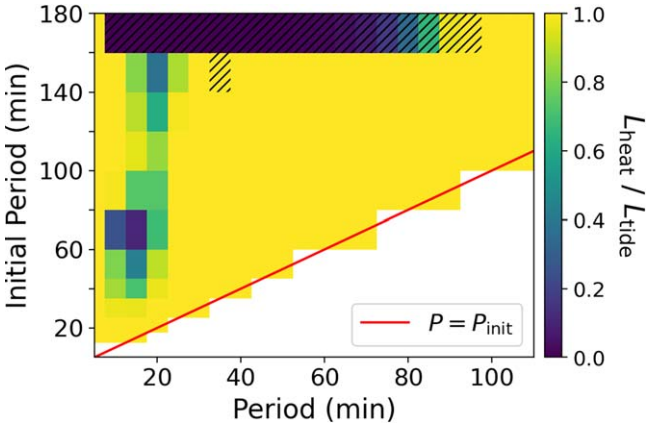

Figure 5. Same as Figure 3, but for a 0.45 $M_\odot$ WD model in a binary.

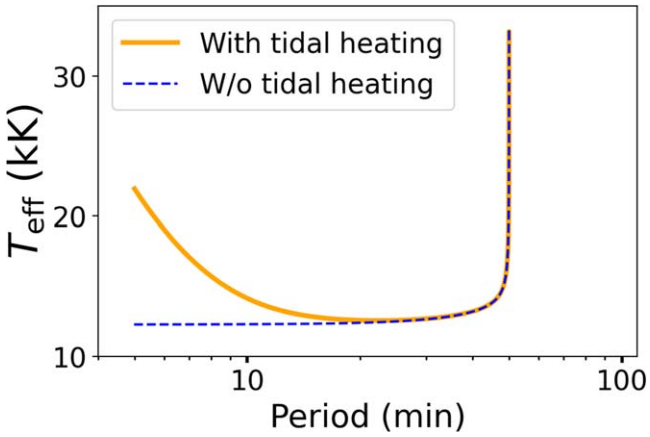

Figure 6. The effective temperature for a 0.25 $M_\odot$ WD, with and without tidal heating, as a function of orbital period. The model moves from right to left toward shorter orbital periods as the binary inspirals. The companion mass is fixed at 0.3 $M_\odot$.

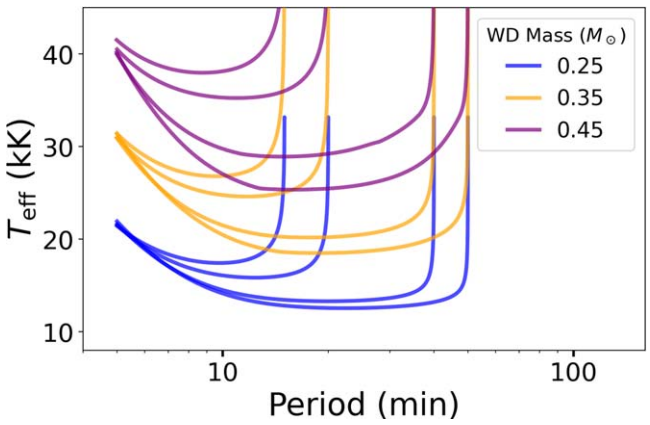

Figure 7. The evolution of effective temperature vs. orbital period for a grid of WD models undergoing tidal heating. Models of same color are of the same mass. The models begin evolution in a binary at orbital periods of 15, 20, 40, and 50 minutes. The companion mass is fixed at 0.3 $M_\odot$.

simulation may encounter regions where the traveling-wave regime is more or less appropriate. The most self-consistent simulations occur for horizontal slices that are completely yellow in color, where all the wave power is always deposited. When $L_{heat}/L_{tide} < 1$, the wave is encountering the edge of the cavity due to either ω^2 rising above L_l^2 (unhatched; "Lamb cavity") or ω^2 rising above N^2 (hatched; "Brunt cavity").

There are several trends evident in Figures 3, 4, and 5. The hatched "Brunt cavity" region occurs for cool WDs in binaries initialized at long orbital periods, because WDs with $T_{eff} \lesssim 10{,}000$ K develop a deep surface convective zone with $N^2 < 0$. Less massive He-core WDs cool faster and have slower orbital decay, meaning that the hatched region is pushed to lower initial periods for lower-mass WDs.

The darkest unhatched "Lamb cavity" regions tend to occur for orbital periods of ≈15–30 minutes, where the tidal frequency ω is largest, which moves the cavity's outer boundary inward and also increases the length scale for damping (Equation (11)). However, at shorter periods, two effects can occur: First, the WD temperature begins to increase as a result of tidal heating, meaning that radiative damping becomes stronger, which in turn makes more heat dissipate out of the wave before it reaches the cavity's edge. Second, the increasing power carried by the wave means that wave breaking is more likely to occur and dissipate more energy within the cavity. These effects are responsible for the yellow region at short orbital periods, where models are nominally again in a traveling-wave regime, despite our traveling-wave model potentially failing at earlier periods in their evolution. At a given period, WDs are cooler for a longer initial orbital period, and radiative damping will be weaker, explaining why, in general, colors are darker moving vertically upward within the unhatched "Lamb cavity" region.

In general, we find that there is still a fairly large parameter space where the traveling-wave regime is valid. WDs in binaries with shorter initial orbital periods are more likely to be in this regime. Higher-mass WDs have a wider range of initial orbital periods where the traveling-wave approximation is valid. Previous work has demonstrated that most DWDs are likely born from the CE channel at orbital periods shorter than 2 hr (Brown et al. 2016), and many at less than 1 hr (Scherbak & Fuller 2023). Therefore, the traveling-wave regime is likely a good approximation for the evolutionary histories of some systems. In the remainder of this work, we run models by implementing the traveling-wave response and only depositing energy within the propagation cavity, but we discuss which models are most valid.

4. Tidal Heating: Simulations and Observed Systems

Figure 6 demonstrates the effect of tidal heating on a WD's surface temperature as the DWD binary evolves from 50 minutes to shorter orbital periods. Note from Figure 3 that this simulation (WD mass 0.25 $M_\odot$, initial period 50 minutes) is likely always in the traveling-wave regime. The magnitude of the heating increases with decreasing orbital period because the tidal potential driving the wave is stronger. The temperature of the primary WD is predicted to be much higher at very short periods (a difference of >10,000 K at an orbital period of 5 minutes) compared to the case where tidal heating is neglected. We find that there is a negligible increase in the radii of our tidally heated models. Significant heating begins at periods $\lesssim$15 minutes, corresponding to a GW inspiral time $\lesssim$2 Myr for the component masses. Thus, the heating generally occurs over a short timescale compared to the WD's age. In the following, we present similar results for a grid of WD models.

Figure 7 shows tidal heating for a grid of WDs of different masses initialized in binaries of different initial orbital periods. For simplicity, we show initial orbital periods of

Table 1
Properties of the WD Binaries We Model

Name (1)	$P_{\rm orb}$ (minutes) (2)	M_1 ($M_\odot$) (3)	M_2($M_\odot$) (4)	$T_{\rm eff,1}$ (K) (5)	$T_{\rm eff,2}$ (K) (6)	$P_{\rm birth}$ (minutes) (7)
ZTF J1539+5027 (1)	6.91	$0.21^{+0.014}_{-0.015}$	$0.61^{+0.017}_{-0.022}$	<10, 000	48,900 ± 900	not modeled
ZTF J2243+5242 (2)	8.80	$0.323^{+0.065}_{-0.047}$ (LC)	$0.335^{+0.052}_{-0.054}$ (LC)	26, 300^{+1700}_{-900} (SED)	19, 200^{+1500}_{-900} (SED)	10–26
		$0.317^{+0.074}_{-0.074}$ (Spect)	$0.274^{+0.047}_{-0.047}$ (Spect)	26, 520^{+130}_{-130} (Spect)	19, 670^{+100}_{-100} (Spect)	
SDSS J0651+2844 (3, 4, 7)	12.75	$0.247^{+0.015}_{-0.015}$	$0.49^{+0.02}_{-0.02}$	16,530 ± 200	8700 ± 500	20–30
ZTF J0538+1953 (5)	14.44	$0.45^{+0.05}_{-0.05}$	$0.32^{+0.03}_{-0.03}$	26,450 ± 725	12,800 ± 200	36–44
SDSS J0935+4411 (6, 7)	19.80	$0.312^{+0.019}_{-0.019}$	$0.75^{+0.24}_{-0.23}$	21,660 ± 380	n/a	22–41

Note. Parameters for all the systems we model, including the orbital period, $P_{\rm orb}$, the masses of the two components, M_1 and M_2, and the effective surface temperature of the components, $T_{\rm eff,1}$ and $T_{\rm eff,2}$. Measured parameters are from (1) Burdge et al. (2019), (2) Burdge et al. (2020a), (3) Brown et al. (2011), (4) Hermes et al. (2012), (5) Burdge et al. (2020b), (6) Kilic et al. (2014), and (7) Brown et al. (2016). The last column is our estimate of the birth period, the post-CE orbital period when the younger WD formed (see text for the analysis).

15–50 minutes, although our full grid ranges from 15 to 200 minutes. For the 0.35 and 0.45 $M_\odot$ models initialized at 50 minutes, the traveling-wave regime starts to break down (this is the source of the kink for the bottom-most 0.45 $M_\odot$ curve at about 13 minutes, where, from Figure 5, there is a change from a small fraction of $L_{\rm tide}$ being deposited to a larger fraction being deposited). However, the traveling-wave regime is likely a good approximation for the other models in this plot.

The power carried by the wave, $L_{\rm tide}$, scales with WD mass approximately as $M_1^{17/6}$ (Fuller & Lai 2013), so more massive WDs experience greater heating at short periods and have higher temperatures, regardless of their initial orbital period. In addition, more massive WDs have smaller radii, and therefore the effect of tidal heating on $T_{\rm eff}$ will be more pronounced.

We also compare our quantitative predictions for $T_{\rm eff}$ to observed ultra–short-period DWD systems. The properties of these systems are summarized in Table 1. Note also that these are the five detached shortest-period LISA verification binary systems discussed in Kupfer et al. (2023). In this work, we only simulate tidal heating in the younger, more recently formed WD, treating the other as a point mass. If only one WD has a mass consistent with a He-core WD, we assume that is the younger because its progenitor star likely evolved second (although this may not always be true). If there are two He-core WDs, we assume that the hotter one is the younger. In Table 1, we define M_1 as the WD we assume is younger and for which we are modeling tidal heating.

Figures 8–11 show a comparison of our WD models, with and without tidal heating turned on, to the observed $T_{\rm eff}$ of systems in Table 1. We do not seek to exactly find the best set of models that match to the observed characteristics, but we compare relevant models with and without tidal heating and quantify the difference between them.

In Figure 8, showing the 8.8-minute system ZTF J2243, the models that best match the observed $T_{\rm eff}$ of the WD primary correspond to 0.35 $M_\odot$ WDs. Both simulations with and without tidal heating can match the data—for instance, the two 0.35 $M_\odot$ models starting at a 15-minute period are consistent with the error bar. Models starting at 30 minutes or greater are not hot enough to match the data, even with tidal heating turned on. Therefore, a WD that cools sufficiently is unable to be heated by tides to the observed hot temperature (≈26,000 K). Comparing the hottest two pairs of 0.35 $M_\odot$ models (the top two pairs of orange curves), the increase in luminosity is about 20% with tidal heating implemented. Thus, tidal heating is a relatively small fraction of the WD primary's energy output.

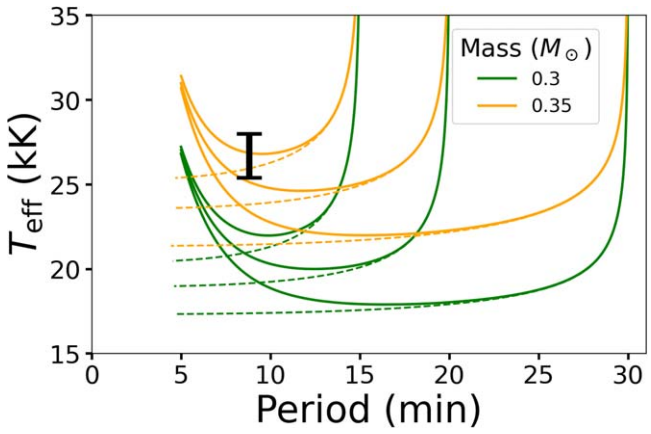

Figure 8. Effective temperature vs. orbital period for a grid of WD simulations, compared to the observed temperature (black error bar) of ZTF J2243's hotter component (mass ≈0.32 $M_\odot$). The models vary in WD mass (differing colors) and initial orbital period of the system, whereas companion mass is fixed at 0.3 $M_\odot$. Dashed lines are models with the same parameters, but with tidal heating turned off.

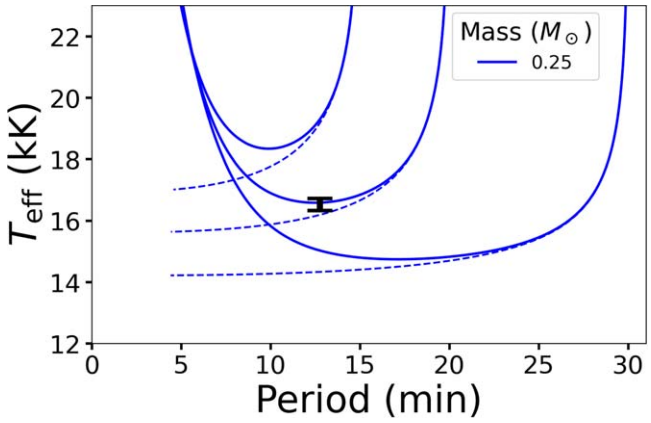

Figure 9. Similar to Figure 8, but for SDSS J0651. The mass of the hotter component, which we fit to, is ≈0.25 $M_\odot$. The companion mass is fixed at 0.5 $M_\odot$.

Figures 9 and 10 show similar results for the 12.8-minute system SDSS J0651 and the 14.4-minute system ZTF J0538. In both cases, the difference between pairs of models with and without tidal heating at the observed orbital period is relatively small, with the change in $T_{\rm eff}$ <1000 K and the change in luminosity between 5% and 10%. For J0651, models starting at 20 minutes match well, but models starting at 15 minutes are

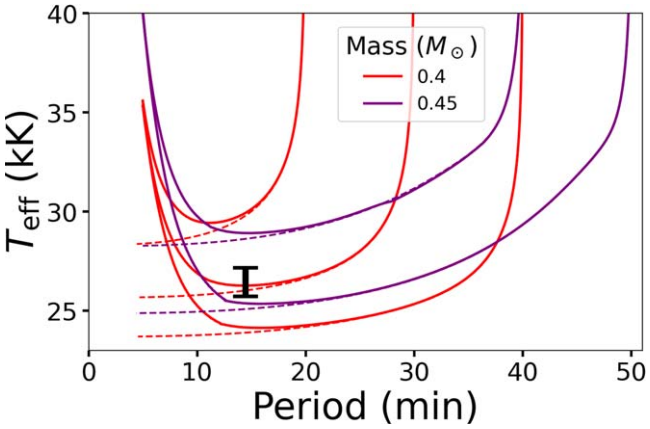

Figure 10. Similar to Figure 8, but for ZTF J0538. The mass of the hotter component, which we fit to, is ≈0.45 $M_\odot$. The companion mass is fixed at 0.3 $M_\odot$.

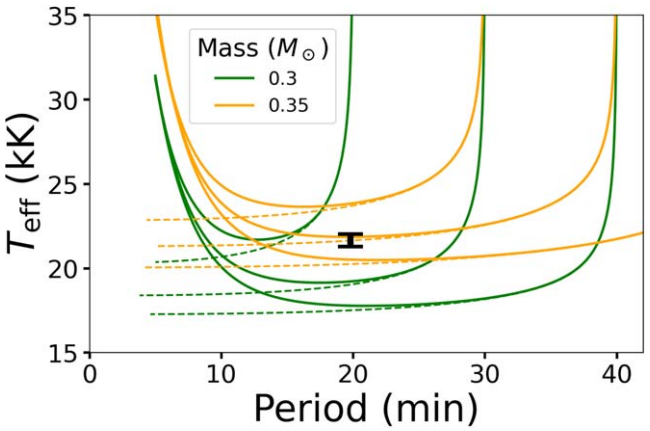

Figure 11. Similar to Figure 8, but for SDSS J0935. The mass of the hotter component, which we fit to, is ≈0.31 $M_\odot$. The companion mass is fixed at 0.75 $M_\odot$.

too hot and models starting at 30 minutes are too cool. For J0538, models starting at 30 minutes match well, but models starting at 20 minutes are too hot and models starting at 40 minutes are too cool. Accounting for tides, therefore, does not appear to greatly alter the parameter space of initial periods that can replicate these systems.

Finally, Figure 11 shows the 19.8-minute system SDSS J0935, the longest-period binary we compare to, and demonstrates that there is little difference between tidally heated and nontidally heated models at orbital periods near 20 minutes.

Note that the models in Figures 8–11 have short initial periods and are therefore mostly in the traveling-wave regime. An exception is the higher-mass, longer initial period (50 minutes) models in Figure 10, for which our treatment may start to break down. Models born at longer orbital periods than plotted are likely in the standing-wave regime and are unlikely to undergo significantly more heating compared to those in the traveling-wave regime. Therefore, since some traveling-wave models already fall below the observed $T_{\rm eff}$, the standing-wave models are unlikely to further the space of models that can match the observed $T_{\rm eff}$ of these four hot WD primaries.

We do not show a plot for the 7-minute binary ZTF J1539, for which the He WD component has a $T_{\rm eff}$ of <10,000 K. The history of this system is uncertain, with mass transfer from the He WD to its companion potentially playing a role (Burdge et al. 2019). It may have also formed via the stable mass transfer channel rather than the CE channel (Li et al. 2019; Chen et al. 2022). Our models tend to predict significantly higher $T_{\rm eff}$ than 10,000 K, regardless of initial orbital period, meaning that our traveling-wave models are incompatible with the low observed temperature. However, we note that if a WD were to cool to <10,000 K, the tidal response is likely in the standing-wave regime, which we do not attempt to model but will involve resonances with g-modes. In our traveling-wave models, the tidal power is deposited near the surface of the WD. In the standing-wave regime, the tidal heating power could be smaller, and the location of heat deposition could potentially be deeper inside the WD. This could allow for much cooler WDs.

5. Discussion

5.1. Implications for Common Envelope Efficiency

Our analysis shows that, for the systems in Table 1, tides are not transforming a cool WD into a hot one, but instead are only slightly heating already-hot WDs. Tidal heating does not significantly alter estimates of the initial orbital period of these ultra–short-period DWD binaries. To better understand the formation history of these systems, it is reasonable to use a grid of nontidally heated models, with varying mass and H envelope mass, to estimate the post-CE periods of these binaries. We performed similar analysis for several DWD systems in Scherbak & Fuller (2023). We follow the same procedure and only briefly outline it here.

We fit a grid of MESA models to the observed radii and $T_{\rm eff}$ of the WD primary to estimate the birth period. As this is also the post-CE period, we thereby obtain the post-CE orbital energy $E_{{\rm orb},\,f}$. We estimate the pre-CE orbital energy $E_{{\rm orb},\,i}$ and the envelope binding energy $E_{\rm bind}$ using a grid of red giant progenitor models whose core mass matches the observed He WD mass. We then combine these to estimate the CE efficiency $\alpha_{\rm CE}$, defined by

$$\alpha_{\rm CE} = \frac{E_{\rm bind}}{E_{{\rm orb},f} - E_{{\rm orb},i}}. \tag{15}$$

Our estimates of the birth period are shown in the rightmost column of Table 1. The birth periods are quite short, significantly less than 1 hr, in agreement with the conclusion of Brown et al. (2016) that most low-mass DWD binaries are born at short orbital periods. It also means that the DWD binaries we model are young.

Figure 12 shows the range of $\alpha_{\rm CE}$ for 10 WD binaries modeled in Scherbak & Fuller (2023) and the four binaries discussed in Figures 8–11. The previously modeled WD binaries are at longer orbital periods >20 minutes. The best-fit range for $\alpha_{\rm CE}$ using these previous 10 systems is from about 0.15 to 0.5 and overlaps well with three of the four new systems. For the most part, we find that these ultra–short-period binaries, which we previously did not model because of the uncertainty of the role of tidal heating, are consistent with a low CE efficiency.

An exception is ZTF J0538, which has an even lower associated range of $\alpha_{\rm CE}$ owing to its short post-CE orbital period and higher-mass WD, which means that the progenitor was more evolved up the red giant branch with a lower $E_{\rm bind}$.

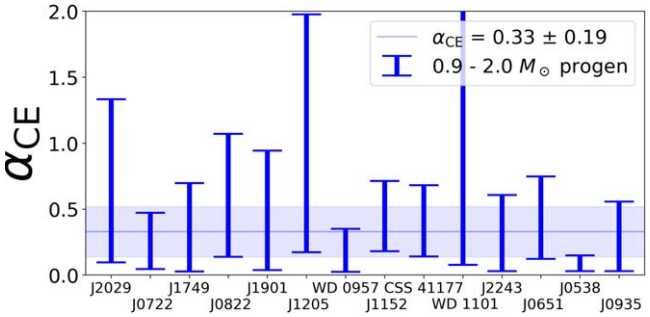

Figure 12. Values of α_{CE} using a grid of He WDs to model the WD primary and assuming that the progenitor is a red giant star from 0.9 to 2.0 $M_\odot$. The horizontal line and shaded region denote a least-squares fit to the ensemble of systems, excluding the rightmost four (the binaries discussed in this work). The other 10 systems used for the fit are longer-period WD binaries modeled in Scherbak & Fuller (2023). The inferred values of α_{CE} for the short-period binaries in this work are consistent with expectations, apart from J0538 (see text for explanation).

However, the mass of the WD primary ($0.45^{+0.05}_{-0.05} M_\odot$) is quite large for a He WD, and it could instead correspond to a low-mass CO-core WD. This requires a significantly different evolutionary history, likely involving a He-burning sdB phase following the CE (Han et al. 2003; Xiong et al. 2017). This would entail a much longer evolution time following the CE event, and hence a longer post-CE orbital period than that listed in Table 1 and a larger value of α_{CE} than that shown in Figure 12.

5.2. Application to CO WDs

This work has focused on tidal heating in He-core WDs, where the companion is either a He or CO WD. A discovery of a short-period binary where both WDs have CO cores would motivate modeling of tidal heating in a CO WD as well. The excitation of outgoing gravity waves in a CO WD (Fuller & Lai 2012) is similar to the He WD case (Fuller & Lai 2013), although the primary location of the gravity wave excitation is instead at the carbon–helium composition gradient. Therefore, most of our modeling can be directly extended to MESA simulations of CO WDs.

The most significant difference would likely be the parameterization of the tidal torque through $F(\omega)$ (Equations (5) and (6)), which we could determine by running the numerical waveform solver on CO WD models. In this work, we found smaller values of $F(\omega)$ compared to those in Fuller & Lai (2013), which used older He WD models. If this trend holds true for CO WDs as well, the results of Fuller & Lai (2012) will be changed somewhat. In particular, the critical period when spin synchronization begins may be shorter, and the magnitude of tidal heating may be higher, than presented in Fuller & Lai (2012). Overall, we expect similar qualitative behavior for CO WD models, with tidal heating becoming significant at periods $\lesssim$10–20 minutes and becoming the dominant source of luminosity premerger.

5.3. Potential Future Observations

The discovery of more ultra–short-period DWD binaries would be invaluable to add to our comparison sample. The enhancement in temperature due to tidal heating increases for shorter orbital periods, so systems with orbital periods $<$10 minutes are better for distinguishing tidally heated and nontidally heated models. Specifically, values of $T_{\rm eff}$ tend to converge for a given WD mass (Figure 7) at the shortest orbital periods before mass transfer, which would be a testable prediction. In addition, discovering more systems at similar periods to the 7-minute binary ZTF J1539 would shed light on whether ZTF J1539's cool component is an outlier, perhaps due to its low mass, or whether there are additional cool WDs for which the tidal heating may be more complicated than modeled here.

In this work, we have only compared to measured values of $T_{\rm eff}$. Measured spin values would be another way to test our models, which predict spin synchronization as a function of orbital period. In some cases, the projected rotation speed, $v \sin i$, could potentially be measured. For complete synchronization, we expect

$$v \sin i \simeq 200 \text{ km s}^{-1} \left(\frac{R_{\rm WD}}{2 \times 10^9 \text{ cm}}\right)\left(\frac{P_{\rm orb}}{10 \text{ minutes}}\right)^{-1} \quad (16)$$

for an edge-on system. This could possibly be measured from high-resolution spectra resolving the non-LTE line cores of DA WDs, or helium lines of DB or DAB WDs.

6. Conclusion

In this paper, we have modeled tidal heating in DWD binary MESA simulations, where the dynamical tidal excitation occurs within helium-core WDs and the companion is a point mass. We approximate the tidal response as traveling gravity waves that are damped in the outer layers of the WD. We run a grid of models varying (1) the mass of the He-core WD M_1, (2) the mass of the companion M_2, and (3) the post-CE orbital period of the WD binary when the second WD formed.

In our simulations, the binary inspirals to shorter periods owing to the emission of GWs. At every time step, we calculate the AM and energy flux carried by the tidally excited waves, which leads to spin-up and heating of the WD. For our grid of WD models, we calibrate the strength of the tidal response using the numerical solver of Fuller & Lai (2013).

The WDs' spins become increasingly synchronized with the orbit at orbital periods $\lesssim$30 minutes. We model heat deposition in the outer layers of the WD, accounting for damping due to radiative diffusion and nonlinear wave breaking. We self-consistently compute the changing WD structure, heating rate, and heating location. The inner edge of wave propagation is the transition between the He core and H envelope, and the outer edge is where the wave becomes evanescent. We determine the fraction of the wave's energy that has been deposited before it reaches the cavity's outer edge. If the fraction is low, our traveling-wave approximation breaks down and the response will instead likely be a standing wave. Figures 3–5 demonstrate where the traveling-wave response is appropriate. In general, hot and young WDs, corresponding to binaries with short initial orbital periods $\lesssim$2 hr, are more likely to be in the traveling-wave regime. The traveling-wave regime extends to longer initial periods for higher-mass WDs ($\sim$0.45 $M_\odot$) compared to lower-mass WDs ($\sim$0.25 $M_\odot$).

At orbital periods $\gtrsim$20 minutes, the WDs follow a cooling track and tidal heating is negligible. However, at shorter orbital periods, the energy flux carried by the tidally excited gravity waves becomes large enough to cause substantial heating. Compared with a nontidally heated model, the enhancement in $T_{\rm eff}$ can exceed 10,000 K at periods of 5–10 minutes. When tidal heating dominates, WDs of the same mass tend to

converge to similar values of $T_{\rm eff}$, despite differences in their previous cooling history.

We compare our tidal heating models to the five shortest-period DWD systems known, with orbital periods ranging from 8 to 20 minutes. Our tidally heated models that match well to the measurements are likely in the traveling-wave regime, but they only cause a mild temperature increase. Both tidally heated and nontidally heated models are capable of reproducing the measured surface temperatures, but only when starting at a similar range of orbital periods. Therefore, uncertainty in tidal heating does *not* lead to a large uncertainty in the binary's initial period. Since tidal heating is a small fraction of these WDs' luminosities, they are intrinsically hot and young, and they were born at periods $\lesssim$45 minutes. The exception to these findings is ZTF J1539's primary, which is cooler than our tidal heating models would predict but has caveats involving mass transfer, its formation history, and the role of standing waves at its cool temperature.

Finally, we reconstruct the values of the CE efficiency parameter $\alpha_{\rm CE}$ that can replicate these systems. Since tidal heating does not significantly impact estimates of the initial (post-CE) period of these ultra–short-period binaries, we perform the same analysis as Scherbak & Fuller (2023), which modeled longer-period WD binaries. For reasonable assumptions of the progenitor star mass, we find that a fairly low value of $\alpha_{\rm CE}$, in the range 0.1–0.5, is necessary to form the ultra–short-period systems. These low values of $\alpha_{\rm CE}$ are consistent with those found in Scherbak & Fuller (2023).

Acknowledgments

We are grateful for support from the NSF through grant AST-2205974. J.F. is thankful for support through an Innovator Grant from The Rose Hills Foundation. We thank the anonymous referee for their useful feedback and suggestions.

Software: MESA (Paxton et al. 2011, 2013, 2015, 2018, 2019), Python. MESA models and files are available in a Zenodo repository (Scherbak & Fuller 2024).

Appendix A
AM Transport

This work has assumed that the WD is rigidly rotating. This requires AM transport between the location where AM is deposited by the outgoing gravity waves and the rest of the WD's interior. We have not performed detailed modeling of AM transport in MESA. Rather, we have estimated the coupling timescale for AM to be transported by a magnetic dynamo and compared that to the spin-up timescale of the WD's interior. For coupling from the WD surface at radius R to a location with internal radius r, we define the AM coupling timescale $t_{\rm coup}(r)$ as

$$t_{\rm coup}(r) = \int_r^R dr' \frac{(R - r')}{\nu(r')}, \tag{A1}$$

where ν is the AM diffusivity found in Fuller et al. (2019), which details a modification to the Tayler–Spruit dynamo (Spruit 2002). It is given by

$$\nu = \alpha^3 r^2 \Omega_s \left(\frac{\Omega_s}{N_{\rm eff}}\right)^2. \tag{A2}$$

We use $\alpha \approx 0.25$ (Fuller & Lu 2022). In calculating ν, we assume that $N_{\rm eff}$ is the full Brunt–Väisälä frequency, as that provides a lower limit on ν and an upper limit on $t_{\rm coup}(r)$. Because our assumption of rigid rotation breaks down for relatively long coupling times, this makes our calculation more conservative.

We define the spin-up timescale $t_{\rm spinup}(r)$ as the timescale to synchronously spin up the layers exterior to r with moment of inertia $I(>r)$. With $\dot{J}_z$ as the full tidal torque as calculated in Equation (5),

$$t_{\rm spinup}(r) = \frac{\Omega I(>r)}{\dot{J}_z}. \tag{A3}$$

We have found that the coupling timescale is generally less than the spin-up timescale, supporting the assumption of rigid rotation. This assumption is better for lower-mass He-core WDs. The assumption of rigid rotation can break down at longer orbital periods $\gtrsim$30 minutes, mainly because the spin rate is smaller and hence the AM diffusivity ν is smaller. However, at longer orbital periods, tidal effects are weaker and deviation from rigid rotation will likely not matter, especially for tidal heating. We find that at short orbital periods the coupling timescale is shorter than the spin-up timescale at most internal radii r, and therefore the WD tends to be rigidly rotating when it is rotating closest to synchronization and undergoing the strongest tidal heating.

Appendix B
Calculation of Wave Breaking

We calculate the radial displacement ξ_r associated with outgoing gravity waves in order to determine when nonlinear wave breaking is likely to occur. Because the power in the wave $L_{\rm tide}$ decreases as the wave moves outward (Equation (14)), $L_{\rm tide}$ is a function of internal radius r. $L_{\rm tide}(r)$ can be related to $\xi_\perp$, the perpendicular displacement, with

$$L_{\rm tide}(r) = 2\sqrt{l(l+1)}\,\frac{\omega^4 \rho r^3 |\xi_\perp|^2}{N}, \tag{B1}$$

and $\xi_\perp$ and ξ_r are related in the WKB approximation via

$$|\xi_r|/|\xi_\perp| = \sqrt{l(l+1)}\,\frac{\omega}{N}. \tag{B2}$$

These formulae will break down if the wave nears the edge of the propagation cavity where ω^2 becomes comparable to L_l^2 (i.e., if the traveling-wave approximation breaks down; Section 3.2.1).

Appendix C
Effect of Hydrogen Envelope Mass on Tidal Heating

He-core WDs can vary in the masses of their H envelopes. We modeled tidal heating for models with a fixed total mass, but varying the mass of the He core and H envelope. Figure 13 demonstrates the evolution of effective temperature for three models of varying H mass, initialized in a binary with the same initial orbital period. Early in the evolution, tidal heating is unimportant, but the models exhibit different cooling behavior based on how thick the H envelope is. When tidal heating dominates at short orbital periods, we find that models with a lower mass of H reach higher values of $T_{\rm eff}$, which is a consistent trend over all our WD models. This trend is not

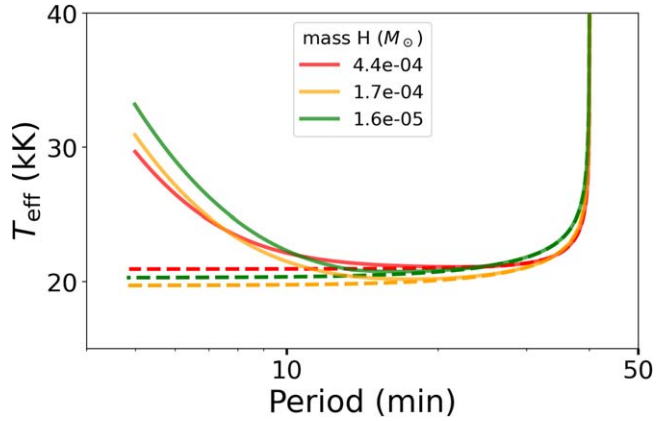

Figure 13. The evolution of effective temperature vs. orbital period for several WD models undergoing tidal heating, all of total mass 0.35 $M_\odot$ but with a varying hydrogen envelope mass. Dashed lines correspond to the same models, but with tidal heating turned off. The companion mass is fixed at 0.3 $M_\odot$.

necessarily true when tidal heating is turned off and models continue to cool.

The main cause for this behavior is the changing radius of the WD, as models with more H have a larger radius (for the models in Figure 13, the radius changes by a factor of ≈10%). The radius affects the tidal heating power $L_{\rm tide}$, which scales with the radius R, the moment of inertia I, and the tidal torque scaling parameter $\hat{f}$ as (see Equation (6) and Fuller & Lai 2013 for a derivation)

$$L_{\rm tide} \propto \frac{I^{8/7}\hat{f}^{-1/7}}{R^{-31/14}}. \quad \text{(C1)}$$

The values of I and $\hat{f}$ can depend on R, but in our models a changing radius barely changes I and moderately changes $\hat{f}$, which hardly affects $L_{\rm tide}$. At short periods, when tidal heating dominates the luminosity, and neglecting the changes in I and $\hat{f}$,

$$T_{\rm eff}^4 \propto \frac{L_{\rm tide}}{R^2} \propto \frac{R^{-31/14}}{R^2} \propto R^{-59/14}. \quad \text{(C2)}$$

In summary, we find that models with a lower mass of H have smaller radii and reach higher $T_{\rm eff}$ when tidal heating is strong at very short orbital periods. However, the variance in $T_{\rm eff}$ due to varying H mass is $\lesssim$10% over a wide range of orbital periods. For the systems that we model, the uncertainties in the total WD mass and initial orbital period of the binary lead to greater uncertainties in $T_{\rm eff}$ (see, e.g., Figure 7). Thus, we do not vary the mass of H in our models for our main analysis. Testing our predictions of the effect of H envelope mass on tidal heating would be difficult, due to both its relatively small influence on $T_{\rm eff}$ and the fact that most WDs do not have measured constraints on their H envelope mass.

ORCID iDs

Peter Scherbak https://orcid.org/0000-0003-4221-9097
Jim Fuller https://orcid.org/0000-0002-4544-0750

References

Brickhill, A. J. 1983, MNRAS, 204, 537
Brown, W. R., Kilic, M., Hermes, J. J., et al. 2011, ApJL, 737, L23
Brown, W. R., Kilic, M., Kenyon, S. J., & Gianninas, A. 2016, ApJ, 824, 46
Burdge, K. B., Coughlin, M. W., Fuller, J., et al. 2019, Natur, 571, 528
Burdge, K. B., Coughlin, M. W., Fuller, J., et al. 2020a, ApJL, 905, L7
Burdge, K. B., Prince, T. A., Fuller, J., et al. 2020b, ApJ, 905, 32
Burkart, J., Quataert, E., Arras, P., & Weinberg, N. N. 2013, MNRAS, 433, 332
Chen, H.-L., Tauris, T. M., Chen, X., & Han, Z. 2022, ApJ, 925, 89
Dan, M., Rosswog, S., Brüggen, M., & Podsiadlowski, P. 2014, MNRAS, 438, 14
Fuller, J. 2017, MNRAS, 470, 1642
Fuller, J., & Lai, D. 2011, MNRAS, 412, 1331
Fuller, J., & Lai, D. 2012, MNRAS, 421, 426
Fuller, J., & Lai, D. 2013, MNRAS, 430, 274
Fuller, J., & Lu, W. 2022, MNRAS, 511, 3951
Fuller, J., Piro, A. L., & Jermyn, A. S. 2019, MNRAS, 485, 3661
Goldreich, P., & Nicholson, P. D. 1989, ApJ, 342, 1079
Han, Z., Podsiadlowski, P., Maxted, P. F. L., & Marsh, T. R. 2003, MNRAS, 341, 669
Hermes, J. J., Kilic, M., Brown, W. R., et al. 2012, ApJL, 757, L21
Iben, I., Jr, Tutukov, A. V., & Fedorova, A. V. 1998, ApJ, 503, 344
Kilic, M., Brown, W. R., Gianninas, A., et al. 2014, MNRAS, 444, L1
Kupfer, T., Korol, V., Littenberg, T. B., et al. 2023, arXiv:2302.12719
Li, Z., Chen, X., Chen, H.-L., & Han, Z. 2019, ApJ, 871, 148
Lorén-Aguilar, P., Isern, J., & García-Berro, E. 2009, A&A, 500, 1193
Nelemans, G., & Tout, C. A. 2005, MNRAS, 356, 753
Paxton, B., Bildsten, L., Dotter, A., et al. 2011, ApJS, 192, 3
Paxton, B., Cantiello, M., Arras, P., et al. 2013, ApJS, 208, 4
Paxton, B., Marchant, P., Schwab, J., et al. 2015, ApJS, 220, 15
Paxton, B., Schwab, J., Bauer, E. B., et al. 2018, ApJS, 234, 34
Paxton, B., Smolec, R., Schwab, J., et al. 2019, ApJS, 243, 10
Piro, A. L. 2019, ApJL, 885, L2
Raskin, C., Scannapieco, E., Fryer, C., Rockefeller, G., & Timmes, F. X. 2012, ApJ, 746, 62
Scherbak, P., & Fuller, J. 2023, MNRAS, 518, 3966
Scherbak, P., & Fuller, J. 2024, Ultrashort-period WD binaries are not undergoing strong tidal heating v1, Zenodo, doi:10.5281/zenodo.10452487
Shen, K. J. 2015, ApJL, 805, L6
Spruit, H. C. 2002, A&A, 381, 923
Xiong, H., Chen, X., Podsiadlowski, P., Li, Y., & Han, Z. 2017, A&A, 599, A54
Yoon, S.-C., Podsiadlowski, P., & Rosswog, S. 2007, MNRAS, 380, 933
Yu, H., Fuller, J., & Burdge, K. B. 2021, MNRAS, 501, 1836
Yu, H., Weinberg, N. N., & Fuller, J. 2020, MNRAS, 496, 5482
Zahn, J. P. 1975, A&A, 41, 329
Zahn, J. P. 1977, A&A, 57, 383
Zahn, J.-P. 2008, in EAS Publ. Ser. 29, Tidal Effects in Stars, Planets and Disks, ed. M.-J. Goupil & J.-P. Zhan (Les Ulis: EDP Sciences), 67